Pisano *et al. Journal of Translational Medicine* (2025) 23:1192
https://doi.org/10.1186/s12967-025-07162-2

Journal of Translational Medicine

RESEARCH Open Access

Insights into spheroid formation: interaction of ovarian cancer cells with macrophage populations in the tumor microenvironment

Simone Pisano[1,2], Yajaira Sofia Jimenez[1], Paul Rees[3], Jing Xiao[4], Deyarina Gonzalez[2], Robert Steven Conlan[1,2] and Bruna Corradetti[1,4,5*]

Abstract

Background Treating advanced ovarian cancer (OC) is challenging due to the immunosuppressive tumor microenvironment. This study investigates tumor-immune cell interactions using organotypic spheroid models that simulate the in vivo microenvironment.

Methods A dual-model spheroid system was established combining serous adenocarcinoma SKOV-3 cells with monocytes, pro-inflammatory (MΦ1) or anti-inflammatory (MΦ2) macrophages, or their derived exosomes (EXOs). In Model A, immune cells or EXOs were co-seeded with tumor cells to replicate early heterotypic aggregation. In Model B, immune cells or EXOs were introduced 24 h post-spheroid formation to simulate immune infiltration into established spheroids. Spheroid morphology was quantified by diameter and circularity, while the distribution of immune cells and EXOs was assessed via fluorescence intensity profiling in 2D and 3D. epithelial-to-mesenchymal transition (EMT) marker expression was analyzed to assess tumor cell phenotypic changes.

Results Spheroids formed with SKOV-3 cells and ThP-1 monocytes developed a dense monocyte-enriched outer layer. Macrophage subtypes differentially influenced spheroid morphology: MΦ2 macrophages promoted the formation of multiple, loosely organized spheroids and increased N-cadherin expression, indicative of enhanced EMT. Similarly, MΦ-EXOs modulated EMT marker expression, underscoring the contribution of both direct cell interactions and paracrine signaling in regulating spheroid dynamics.

Conclusions Macrophages and their exosomes play a critical role in modulating the architecture and functional behavior of spheroids, reflecting two key aspects of OC progression: the formation of immune cell-enriched spheroids in ascitic fluid and tumor-immune interactions at peritoneal metastatic sites. This model provides a clinically relevant platform for preclinical testing of therapeutic strategies targeting peritoneal dissemination in OC.

Keywords Ovarian cancer, Immune cells, Macrophages, Exosomes, Spheroids, Metastatic processes, Image analysis

---

*Correspondence:
Bruna Corradetti
bruna.corradetti@bcm.edu
[1] Department of Nanomedicine, Houston Methodist Research Institute, Houston, TX, USA
[2] Centre for NanoHealth, Swansea University Medical School, Swansea, UK
[3] College of Engineering, Swansea University, Bay Campus, Swansea, UK
[4] Center for Precision Environmental Health, Baylor College of Medicine, Houston, TX, USA
[5] Department of Medicine, Section Oncology/Hematology, Baylor College of Medicine, Houston, TX, USA

Introduction

Ovarian cancer (OC) is widely recognized as a heterogeneous disease in which unique histological types arise from different tissues. High-grade serous ovarian cancer (HGSOC) is the most common epithelial OC subtype and is believed to originate from the epithelium of the fallopian tubes [1], while endometroid and clear-cell subtypes arise from the endometrium [2, 3]. HGSOC presents major challenges in clinical management, particularly due to chemotherapy resistance and the complex immunosuppressive tumor microenvironment (TME) [4]. The heterogeneity of immune microenvironments across different tumor sites within the same patient leads to varying responses to treatment, especially in recurrent cases [5]. While immunotherapy has demonstrated efficacy in treating a range of malignancies [6, 7], its success in advanced ovarian cancer is limited by the immunosuppressive nature and heterogeneity of the tumor microenvironment, as well as the disruption of lymphatic drainage caused by peritoneal cancer cell activity [8]. To develop effective therapeutic strategies and specifically identify the cellular and molecular mechanisms underlying the etiology of this disease a careful selection of appropriate models is required to recapitulate targeted disease subtypes and disease progression. The use of patient derived cells has shed light on the importance of recreating the complexity of OC models in vitro to broaden our knowledge of the pathophysiological behavior of this disease and develop effective treatment strategies [9]. The evaluation of newly developed anti-cancer therapeutics in the preclinical scenario has for a long time relied on in vitro testing using 2D cancer cell cultures, which involve single layer of cells disposed on a plastic surface. Three-dimensional in vitro systems that encompass several aspects of the tumor are steadily replacing 2D cultures [10, 11] to resemble the cellular and molecular events occurring in vivo more closely, since multi-layered components hampers drug penetration [12].

During tumor formation primary cells in the ovaries undergo the epithelial-to-mesenchymal transition (EMT) process that results in a changed phenotype, detaching from a primary tumor and disseminating across the body [13]. Dissemination of these cells from the primary tumor is via ascites, fluid that accumulates in the peritoneal cavity, and has a role in OC [14]. Ascites contains both tumor and non-tumors cells including highly tumorigenic cell spheroids. Many of these cells subsequently form multicellular clusters or spheroids, either through aggregation in the ascitic fluid or by detachment of preformed cell clusters from the primary tumor [15]. These spheroids are considered metastatic units, that are considered the main cause of intraperitoneal metastasis [16]. The tumorigenic spheroids are composed of tumor cells, immune cells and mesenchymal-like cells, where 21% of cells in the spheroids can be CD45 + immune cells [17]. Spheroids are found in the ascitic fluid and spread throughout the peritoneal cavity, contributing to the establishment of secondary tumor sites on the mesothelial layer of the omentum after undergoing the reverse process of mesenchymal-to-epithelial transition [18, 19]. For this reason, spheroids represent the most common systems engineered to mimic (a) spheroids in the ascites and (b) localized metastatic sites. The typical structure of a spheroid consists of a three-layer profile, in which the outside layer consists of proliferating cells with intact nuclei, with the inner two layers composed of quiescent (with minimal metabolic activity but can regain activity after exposure to nutrients) and necrotic cells (with disintegrated membranes and nuclei due to starvation and accumulation of toxic waste) [20]. Intercellular interactions are also recreated in vitro through the use of multicellular models (also defined as organotypic models) [21]. By conducting a multiparametric analysis of the immune landscape within the peritoneal cavity of HGSOC-bearing mice, we recently demonstrated that tumor nodules are enriched in T cells and macrophages (MF) [22]. Indeed, tumor associated macrophages (TAMs) have been the focus of intense research aiming at understanding their role in the formation and spreading of OC multicellular clusters [23]. Notably, patient-derived ascitic spheroids are generally composed predominantly of tumor cells with a minority of infiltrating immune cells - most notably TAMs. Although immune cell percentages vary, even a modest MF presence is significant given their ability to promote chemoresistance, invasion, and modulation of the TME. TAMs are especially prominent: analyses of ascites from ovarian cancer patients found MF present in essentially all spheroids examined [17].

The reciprocal interaction of MF and cancer stem cells within OC spheroids has demonstrated an upregulation of anti-inflammatory (M2) markers in a hanging-drop hetero-spheroid model of OC, which implies a more immunosuppressive behavior and drives chemoresistance [24]. Furthermore, extracellular vesicles (including exosomes, EXOs) and their role in mediating cell-to-cell interactions has sparked interest into the implication of tumor and monocyte/macrophage cells interaction in the creation of an immunosuppressive tumor microenvironment [25, 26]. miRNA (miR-21–3p, miR-125 b-5p and miR-181 d-5p)-driven effects of EXOs derived from SKOV-3 cells (an OC cell line) have been associated to promote a M2-like phenotype in recipient macrophages [26]. Better understanding the interplay between MF and cancer cells in spheroid models may help in unveiling additional mechanisms that drive (or hinder) their metastatic potential. Monocytic cells that contribute to tumor growth and metastasis have also been identified in ovarian cancer TME and continue to be of interest with regards to epithelial OC prognosis [27, 28].

The aim of this study is to evaluate tumor and immune cell interaction within organotypic spheroid models that closely simulates the in vivo microenvironment of spheroids, with emphasis on the effect of differentially induced MF (and the EXOs derived from them), including pro- and anti-inflammatory macrophages (MF1 and MF2, respectively) on the potential of serous adenocarcinoma cells (SKOV-3 cell line) to generate spheroids. To better capture these in vivo dynamics, our study employs a dual-model approach for spheroid formation. In Model a, ovarian cancer cells (SKOV-3) and immune cells (monocytes/ MF and the EXOs derived from them) are co-seeded from the outset, simulating a scenario where heterotypic aggregation occurs early. In Model b, immune cells are added 24 h after tumor cell aggregation, mimicking an infiltration process that may occur after initial spheroid formation, reflecting the detachment mechanism observed in patient samples. This dual approach allows us to examine the differential effects of early versus delayed immune cell incorporation on spheroid morphology, cell–cell interactions, and EMT marker expression. Cell-to-cell interaction was assessed over time by differentially staining cell populations of interest and the impact of immune cells on spheroid formation was quantified in terms of diameter and circularity features. The distributions of immune cell and EXO infiltration throughout the spheroids was analyzed by calculating the fluorescence intensity relative to the center of the spheroid in both 2 and 3D. Finally, the effect of MF and MF-derived EXOs on the EMT markers expression of SKOV-3 cancer cells was explored. By integrating established methodologies for 3D culture with insights from patient-derived spheroid studies, our work seeks to provide a reductionist yet clinically relevant model. In doing so, we aim to elucidate how macrophages and their secreted EXOs influence spheroid formation, potentially offering new mechanistic insights into OC progression and laying the groundwork for future preclinical testing.

Materials and methods

Cell lines and cultures

Serous adenocarcinoma cells (SKOV-3 cell line, RRID: CVCL_0532) were purchased from Sigma-Aldrich. SKOV-3 cells were cultured in McCoy's media (Gibco) supplemented with 10% Fetal Bovine Serum (FBS, ThermoFisher) and 1% Penicillin/Streptomycin (P/S, ThermoFisher). Cells were incubated at 37 °C in a humidified 5% CO_2 atmosphere and subcultured when 80–90% confluent. ThP-1 monocyte cells were purchased from ATCC® (RRID: CVCL_0006) and grown in Roswell Park Memorial Institute (RPMI)-1640 media supplemented with 2 mM L-glutamine adjusted to contain 1.5 g/L sodium bicarbonate, 4.5 g/L glucose, 10 mM HEPES, 1.0 mM sodium pyruvate (ATCC) and FBS 10%. To generate macrophages (MF), 5×10^6 ThP-1 cells were seeded in T75 petri dish plates and treated with 320 nM phorbol-12-myristate-13-acetate (PMA, Sigma-Aldrich) for 24 h. Similarly, pro-inflammatory macrophages (MF1) were obtained by seeding the same number of ThP-1 cells and treating them with PMA for 6 hrs followed by incubation with 100 ng/mL lipopolysaccharide (LPS, ThermoFisher) and 20 ng/mL IFN-γ (R&D Systems) for 18 h. Anti-inflammatory macrophages (MF2) were obtained by treating ThP-1 cells with 320 nM PMA for 6 hrs and then culturing them with PMA plus 20 ng/mL IL-4 (R&D Systems) and 20 ng/mL IL-13 (R&D Systems) for 18 h [29]. Culture conditions were established at 37 °C and 5% CO_2. Differentiated ThP-1 cells were detached using ice cold Macrophage Detachment Solution (PromoCell GmbH) according to manufacturer's instructions. This solution is specifically designed for the gentle detachment of adherent macrophage-like cells.

Liquid overlay SKOV-3 spheroids optimization

Spheroids were generated following the liquid overlay method [30]. Briefly, 96-well plates (Thermo Scientific) were prepared by first coating each well with 50 µl of 2.5% (w/v) low-melting-point agarose gel (Agarose Low EEO, Melford) using a multichannel pipette. The agarose was heated until fully dissolved and allowed to cool to approximately 37 °C before being pipetted into the wells. The coated 96-well plates were then sterilized under UV light for at least 30 min. For spheroid formation, SKOV-3 cells were detached from the culture plates using Trypsin-EDTA solution (0.25%) and counted using a hemocytometer or an automated cell counter. Cells were diluted to a final concentration of 6,000 cells per 200 µl of complete media (McCoy's media supplemented with 10% FBS and 1% P/S). This cell suspension was added to each well containing the agarose-coated surface. Plates were then gently shaken to ensure an even distribution of cells and incubated under standard conditions (37 °C in a humidified 5% CO_2 atmosphere). Spheroids were cultured overtime and representative bright field images of SKOV-3 spheroids were taken at different time points (24, 48, 72 and 96 h).

Bright-field microscope imaging, ImageJ processing analysis and Immunofluorescence

Spheroids and macrophages were visualized using a Carl Zeiss Microimaging System, and images at different time points were taken with an Axiocam ERc5s camera (Zeiss). Images were processed through the opensource software ImageJ (version 2.1.0/1.53c, RRID: SCR_003070). The diameter of the spheroids was assessed through the "set scale" and "measure" options.

The circularity of the spheroids ($n = 8$/group) was calculated based on the equation: Circularity = 4π (area/perimeter2). This equation generates a value from 0 to 1, where 1 indicates a perfect circle and as the value approaches 0, this indicates an increasingly elongated polygon. ImageJ was used to measure the midpoint width/cell perimeter ratio according to previously reported procedures to assess the phenotypical change of differentiated MFs [31, 32]. Briefly, cell perimeters and midpoint widths were traced manually and measured in pixel units using the ImageJ functions. The ratio of width versus perimeter was obtained for each cell ($n = 40$) and the mean values, standard deviations, and one way ANOVA (with Tukey post-hoc analysis for multiple comparisons) were calculated. Immunofluorescence staining was performed to detect and characterize MF, MF1, and MF2 populations based on the expression of specific markers. Cells were fixed with 4% paraformaldehyde for 15 min at RT. After blocking with 5% bovine serum albumin for 1 h, cells were incubated overnight at 4 °C with primary antibodies against CD68 (MF) (BioLegend Cat# 333805, RRID: AB_1089055), CD80 (MF1) (BioLegend Cat# 305219, RRID: AB_2291403), and CD163 (MF2) (BioLegend Cat# 333613, RRID: AB_2562640). CD68 staining required permeabilization with 0.1% Triton X-100 for 10 min before antibody incubation. To visualize the cytoskeleton, cells were stained with Phalloidin conjugated to Alexa Fluor 488 for 30 min, while nuclei were counterstained with DAPI for 5 min. Confocal microscopy was performed to acquire images, and the expression patterns of CD68, CD80, and CD163 were analyzed to confirm the presence and distribution of the respective macrophage populations.

Exosomal preparations

Exosome isolation

Exosomes were isolated from the media conditioned by ThP-1 cells and macrophages, including MF, MF1, and MF2 following established protocols [33, 34]. 4×10^6 ThP-1 cells were seeded and differentiated as reported above in RPMI-1640 media containing exosome-depleted FBS (Gibco). Upon differentiation, media was collected and centrifuged at 500 x g for 5 min to remove cellular components, followed by centrifugation at 2000 x g for 30 min to eliminate any remaining debris. The supernatant was then transferred to a clean tube and filtered through a 0.22 µm PES membrane filter (CellTreat) and further concentrated using 10 kDa Amicon ultra centrifugal filters (Millipore) through centrifugation at 4000 x g for 15 min. Total exosome isolation reagent (Invitrogen) was added in a 1:2 volume ratio to the media obtained after the Amicon centrifugation process. The solution was mixed, vortexed for 30 s and then incubated overnight at 4 °C. The following day, samples were centrifuged at 10,000 x g for 1 h at 4 °C. The pellet was subsequently resuspended in 0.22 µm filtered PBS. Exosomal suspension was stored at −80 °C.

Exosome physiochemical characterization

Exosomes were characterized for their size and concentration using a Nanosight NS300 (Malvern) and analyzed with the software version NTA 3.3 Dev Build 3.3.301. A 200X dilution of exosomes in PBS was prepared for each sample. Briefly, 3 videos of 60 s each were recorded for each sample (with a frame rate of 24 FPS (frames per second) and a flow rate of infusion of 20 arbitrary units), and the threshold was kept constant at 5. Around 25–30 particles per frame was the number identified before running the analysis. All the experiments were performed using different batches of exosomes, and a one-way ANOVA with Tukey post-hoc analysis for multiple comparisons was performed. Size and concentration measurements were performed using 11 different exosomal batches.

CD63 quantification

The identification of CD63$^+$ exosomes was performed as previously described [33] using the antibody-based ExoELISA-ULTRA Complete Kit (SystemBio), following the manufacturer's instructions. Briefly, exosomes isolated from ThP-1, MΦ, MΦ1, and MΦ2 populations were loaded onto a 96-well plate provided with the kit, and CD63$^+$ particle numbers were quantified against a pre-set exosome standard curve.

Spheroids co-cultures: SKOV-3 and immune cells and derived exosomes

Spheroids were generated mixing ovarian cancer cells (SKOV-3 cells) and immune cells (ThP-1 or ThP-1 derived MF, MF1, and MF2 macrophages). The co-culturing process involved two separate approaches. In the first approach (*Model a*), 6,000 SKOV-3 cells and 2,000 immune cells (either ThP-1, or MF, MF1, MF2) were added to a 96-well liquid overlay plate in a 200 µl volume in a 3:1 ratio. In the second approach (*Model b*), immune cells were added after 24 h from SKOV-3 cells seeding (at which point spheroids had already formed). Co-cultured spheroids were grown for up to 96 h and used for downstream applications. Exposure of SKOV-3-derived spheroids to EXOs (1×10^8/condition) was also achieved following *Model a* and *b*: addition of EXOs (1×10^8/condition) occurred either at time 0 or after 24 h from SKOV-3 seeding.

Spheroid viability

SKOV-3 cells were cultured to form three-dimensional spheroids and subsequently incubated in co-culture with selected immune cell populations (ThP-1, MΦ, MΦ1, and MΦ2) to assess the impact of immune cells on spheroid proliferation. Co-cultures were maintained for 48 h, after which spheroid viability was quantified using the Alamar Blue Cell Viability Reagent (Thermo Fisher Scientific). To determine the impact of EXOs, SKOV-3 spheroids were cultured for 96 h in the presence of ThP-1 cell–derived EXOs, and cell viability was assessed using the CellTiter-Glo Luminescent Cell Viability Assay (Promega) according to the manufacturer's protocol. All data are reported as percentage values normalized to SKOV-3 spheroid–only controls.

Confocal imaging and real time monitoring

Before being seeded to form co-cultured spheroids, SKOV-3 and immune cells were separately stained using PKH67 green fluorescent and PKH26 red fluorescent live cell stains (Sigma-Aldrich). Similarly, immune cell-derived EXOs were stained with PKH67 live cell kit following manufacturer's instructions. In the case of SKOV-3/ MΦ co-cultures, single-plane images were taken at 24, 48, 72 and 96 h time points at a 10X magnification using an Invitrogen^{TM} EVOS^{TM} FL Auto Imaging System. Live-cell videos were acquired over the first 48 h of co-culture. Fluorescent signals were detected through the FITC and RFP channels and merged with bright field images. Similarly, in the case of SKOV-3/MΦ-derived EXOs, images were taken at 24 and 48 h at 20X and 40X magnifications, respectively. An Olympus FV3000 IX83 confocal microscope was used to obtain z-stack images (11 z-steps per sample). The FITC and RFP channels were used to detect the green (excitation 488 nm, emission 500–540 nm) and the red signals (excitation 561 nm, emission 570–670 nm), respectively. Images obtained with the Olympus microscope were processed using ImageJ software to quantify exosomal fluorescent intensity (using the "mean grey value" option of the software) of each Z-stack. In ImageJ processing, green and red signals were split into separate channels, and threshold was set automatically and applied for each signal. The mean grey value was then measured in a fixed area of 22,500 μm^2.

Analysis of immune cell/EXO distribution in the spheroid

Segmentation of the individual SKOV and macrophage cells using the fluorescence markers is challenging when a spheroid has formed due to the proximity of the cells and the 3D architecture. To determine the distributions of the two different entities constituting the spheroids (immune cells or EXOs and SKOV cells), individual pixels were analyzed in corresponding timelapse (Videos 1–8 for cell-to-cell interaction) and fluorescent images for EXO-to-cell interaction, respectively. Fluorescence z plane images ($n = 11$) were thresholded to determine green (immune cells) and red (SKOV-3) pixels. Rather than analyzing the location of the cell centroid, every pixel was analyzed to obtain the distributions. This approach allows us to achieve the same outcome but without the need to segment individual cells. The distance distribution of each pixel (cell) from the center of the spheroid was also determined to evaluate the degree of infiltration. This is complicated by the 'flat spheroid' geometry and used two methods to visualize the distribution of (pixels) cells. To visualize the true 3D distribution, the spheroid was projected onto a true hemisphere. The z-axis was scaled using the radius of spheroid determined at lowest z-plane. The 3D Euclidean distance from the center was subsequently found and results displayed as histograms.

Gene expression analysis

The quantification of mRNA expression was performed to confirm specific immune cell phenotype and to assess differences in EMT markers upon SKOV-3 exposure to immune cells following *Model a*. Total RNA was extracted from immune cells (ThP-1 and macrophages) and spheroids for each co-cultured subgroups using TRIzol™ Reagent (Invitrogen) according to the manufacturer protocol. cDNA synthesis was performed through the High-Capacity RNA-to-cDNA™ Kit (Applied Biosystems) using a T100™ Thermal Cycler (Applied Biosystems). Transcribed products were analyzed using commercially available master mix and the appropriate target probes to detect expression of MF (CD68: Hs02836816_g1), MF1 (CXCL10: *Hs00171042_m1*; TNF-*α: Hs00174128_m1*) and MF2 (CD206: Hs00267207_m1; CCL2; Hs00234140_m1)-associated markers on immune cells, and E-CAD (Hs01023895_m1) and N-CAD (Hs00983056_m1) on spheroids on an ABI StepOne plus Detection System (Applied Biosystems). Expression levels were normalized to the reference gene (GAPDH: Hs02758991_g1). Positive control groups for immune cells include macrophages cultured in presence of IL-4 to induce an MF2 phenotype or LPS for the MF1 phenotype. To compare fold-change expressions across immune cell populations, the housekeeping gene-normalized transcripts quantities of MF/ MF1/ MF2 samples were normalized to ThP-1 samples. Levels of EMT marker expression between spheroids co-cultured with macrophages or EXOs were normalized against expression levels found in spheroids generated using only SKOV-3 cells.

Statistical analysis

All statistical analyses were performed using GraphPad Prism 5 (GraphPad Software Inc., RRID: SCR_002798). Normality of data distribution was evaluated using the Kolmogorov–Smirnov test. For comparisons involving two independent groups, unpaired two-tailed Student's t-tests were used. These analyses assumed normally distributed data, equal variances across groups, and independence of observations. For each comparison, t-statistics, degrees of freedom, exact *p*-values, sample sizes, and effect sizes (Cohen's d) with 95% confidence intervals were calculated and reported in the Results section. For comparisons involving more than two groups, a one-way ANOVA was conducted, incorporating one between-subjects factor. Assumptions of normality and homogeneity of variances (Levene's test) were confirmed prior to analysis. The ANOVA included no blocking or within-subject factors. When the main effect was significant, Tukey's multiple comparison test was applied as a post hoc test. All ANOVA results are reported with F-statistics, degrees of freedom, exact p-values, and descriptive statistics (mean ± standard deviation) for each group. A significance threshold of $p < 0.05$ was adopted for all analyses.

Results

Macrophage differentiation

ThP-1 monocytic cells were first differentiated into MF macrophages and then induced to acquire pro- or anti-inflammatory phenotypes. Twenty-four hours from the initiation of differentiation, bright field microscopy images were taken to assess changes in cell phenotype. Interestingly, MF and MF2 showed a noticeable rounded and cobblestone shape, while MF1 cells presented a more elongated, spindle-like phenotype (Supplementary Fig. 1A). To quantify these differences, the midpoint width/cell perimeter ratio was calculated as this parameter quantifies the morphological differences between cells and decreases when cells assume a more elongated shape. MF1 had a significantly lower ratio than MF and MF2 ($p < 0.001$) (Supplementary Fig. 1B). Further characterization identified specific cell markers associated with pro- and anti-inflammatory phenotypes. The mRNA levels of CD68, a marker associated with the M0 phenotype showed a statistically significant increase of 3.16 ± 1 fold in MF cells compared to ThP-1 cells ($p < 0.001$) (Supplementary Fig. 1C). After confirming the M0 phenotype, the presence of MF1 and MF2-specific markers was evaluated. MF1-associated markers (CXCL10 and TNF-α) were found at significantly higher levels in MF1 compared to MF (considered as the control) (Supplementary Fig. 1D). TNF-*a* showed a fold increase of 2.57 ± 0.84 and 6.04 ± 2.01, after 48 and 72 h induction, respectively. For CXCL10, expression values were 1326.49 ± 210.1 and 334.68 ± 45.23, for 48 and 72 h, respectively. In the case of anti-inflammatory markers, CD206 expression was found to be higher in MF2 than MF with a 23.97 ± 2.01- and 11.72 ± 3.14-fold increase at 24 and 48 h (Supplementary Fig. 1E). A similar trend was also seen when analyzing the second MF2-associated marker (CCL2), for which expression values were found to be 12.37 ± 2.14 and 68.46 ± 13.01, respectively. Immunofluorescence staining successfully identified M0, M1, and M2 macrophage populations based on the expression of CD68, CD80, and CD163, respectively (Supplementary Fig. 1F).

Exosomal preparations from immune cells

EXOs were purified from ThP-1 monocytic cells, MF, MF1 and MF2 and characterized for their size and concentration profiles. Nanosight analysis showed variations in the size of EXOs derived from different macrophage phenotypes (Supplementary Fig. 1G). EXOs derived from ThP-1 cells showed a size of 92.5 ± 12.4 nm which was significantly smaller than differentiated macrophages. EXOs from MF displayed a size of 118.8 ± 19 nm ($p < 0.01$), those from MF1 and MF2 were found to be 127 ± 6.7 nm ($p < 0.001$) and 108 ± 6.7 nm, respectively. Variations in particle concentration values were also observed, with the highest concentration of EXOs being purified from MF cells ($1.16 \times 10^{10} \pm 7.45 \times 10^9$ particles/mL) compared to ThP-1 ($6.70 \times 10^9 \pm 3.92 \times 10^9$ particles/mL, $p < 0.01$), MF1 ($4.36 \times 10^{10} \pm 1.18 \times 10^{10}$ particles/mL, $p < 0.05$) and MF2 cells ($1.23 \times 10^9 \pm 3.89 \times 10^9$ particles/mL) (Supplementary Fig. 1H). All exosome preparations showed expression of the exosomal marker CD63, confirming their identity as extracellular vesicles (Supplementary Fig. 1I). These results, together with NTA-based size distribution and particle concentration data, validated the quality and comparability of the exosome samples used in co-culture experiments.

Organotypic SKOV-3 spheroid cultures and viability assessment following immune cell or EXO exposure

Bright field images of SKOV-3 spheroids produced using the liquid overlay method were taken overtime (Supplementary Fig. 2A) and analysis was performed to determine diameter and circularity. Our data show that spheroid diameter significantly diminished over time from 488 ± 12.21 µm at 24 h to 430.75 ± 23.61 µm at 48 h ($p < 0.01$), 430.93 ± 26.47 µm at 72 h ($p < 0.001$) and 410.53 ± 16.27 µm 96 h ($p < 0.001$), respectively (Supplementary Fig. 2B). Furthermore, the level of circularity of the spheroids significantly increased over time, from 87.8 ± 3.1% at 24 h to 93 ± 1% at 48 h ($p < 0.01$), 92.9 ± 1.2% at 72 h ($p < 0.01$) and 93.1 ± 1.3% at 96 h ($p < 0.001$) (Supplementary Fig. 2C). Co-culture of SKOV-3 spheroids with immune cell populations resulted in increased viability compared to SKOV-3 spheroids cultured alone, which were set as 100% (Supplementary Fig. 2D). The presence of MF induced the highest viability (161.4%), followed by MF1 (155.8%) and ThP-1 cells (138.3%). Spheroids co-cultured with MF2 exhibited a comparatively lower viability (112.8%) than the other immune cell co-cultures, yet values remained above the SKOV-3 spheroid–only control. To evaluate the contribution of secreted factors, SKOV-3 spheroids were treated with ThP-1–derived EXOs and monitored over 96 h

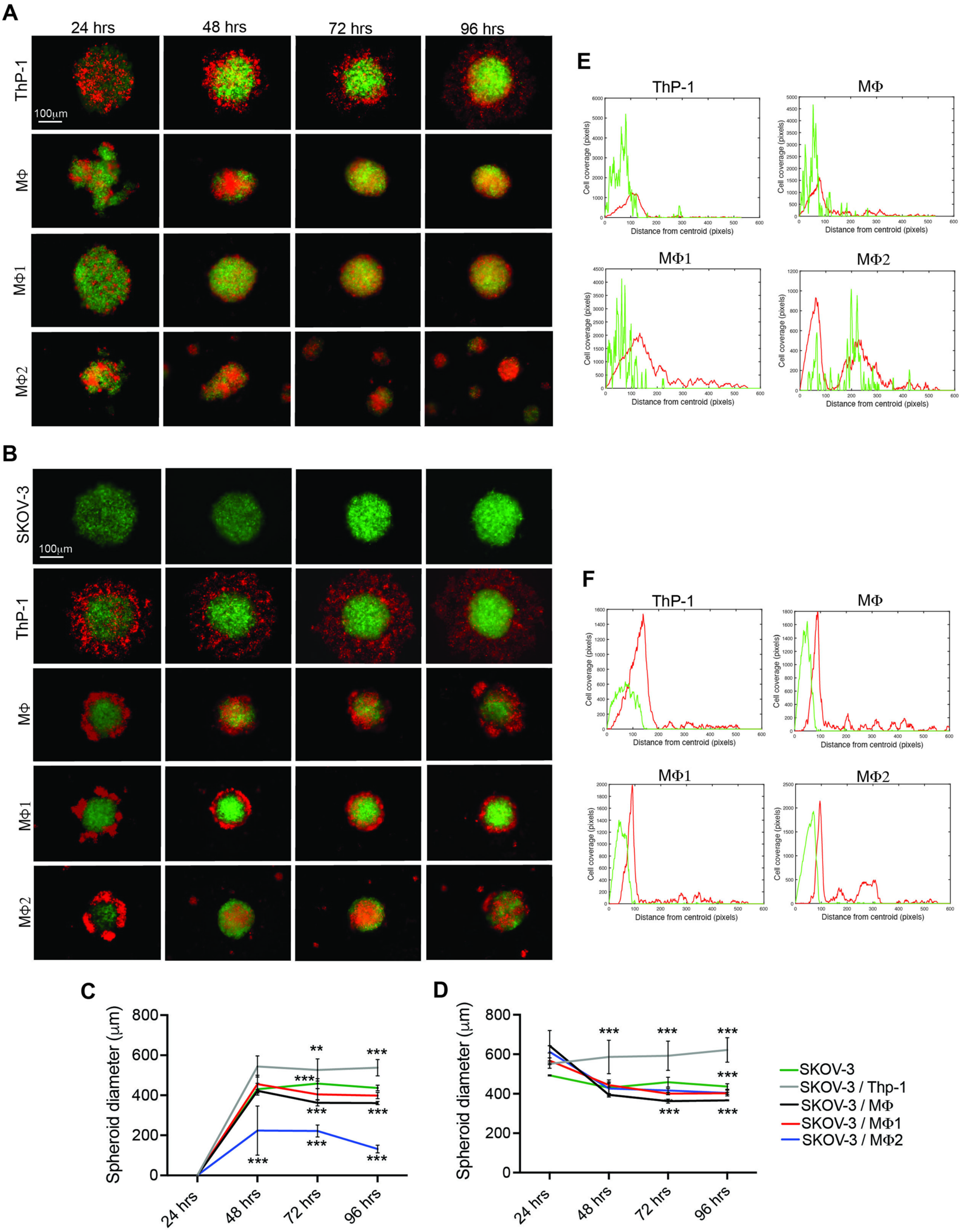

Fig. 1 (See legend on next page.)

(See figure on previous page.)

Fig. 1 Organotypic culture of SKOV-3 and immune cells. Spheroid formation following *Model a* (immune and cancer cells were mixed at time 0, **A**) and *b* (immune cells were mixed after 24 h from forming spheroids, **B**). SKOV-3 cells and immune cells (Thp-1, MΦ, MΦ1, and MΦ2) were fluorescently labelled with PKH67 (green) and PKH26 (red), respectively. Pictures were taken using an EVOS^{TM} FL Auto Imaging System at 0, 24, 48, 72 and 96 h from cell seeding. Scale bar: 1000 µm. Spheroid diameter (µm) measurements performed on ovarian cancer and immune cell co-cultures following *Model a* (**C**) and *b* (**D**). Results obtained from three biological replicates. Statistically significant differences compared to SKOV-3 only spheroids (*** $p < 0.001$). Histograms show immune cell distribution across the spheroids following *Model a* (**E**) and *Model b* (**F**) determined by the total fluorescence intensity relative to the 2D Euclidean distance from the center of the spheroid (for the lowest z-plane) at the latest time point. Green and red lines depict SKOV-3 and immune cells, respectively

(Supplementary Fig. 2E). Cell viability was consistently maintained at levels comparable to control spheroids, with values ranging from 110.9% at 24 h to 99.7% at 96 h.

A reductionist organotypic model was developed by co-culturing SKOV3 cells with macrophages to assess the potential interference of immune cells in the natural spheroid-forming capability of cancer cells. Fluorescently labelled SKOV-3 cells (green) were co-cultured with THP-1 monocytes, MΦ, MΦ1, or MΦ2 (red) under two experimental models: (a) direct mixing of immune cells with SKOV-3 cells at the time of seeding (*Model a*) or (b) addition of immune cells 24 h after SKOV-3 spheroid formation (*Model b*). Representative confocal images were acquired at 24, 48, 72, and 96 h to monitor spheroid morphology and cell distribution. In *Model a* (Fig. 1A), the incorporation of immune cells at the time of seeding differentially influenced spheroid organization depending on the immune cell type. When SKOV-3 cells were combined with ThP-1 monocytes, a monocyte-rich corona began to assemble around the spheroid by 48 h (Video 1), with a progressively clearer separation between the two populations. Monocytes localized predominantly to the spheroid periphery, while SKOV-3 cells occupied the core. In contrast, both MΦ and MΦ1 were evenly distributed throughout the spheroid, forming a mixed-cell uniform structure. Notably, MΦ delayed spheroid compaction compared with MΦ1 (Video 2 vs. Video 3), but ultimately produced a more compact spheroid characterized by tighter SKOV-3 cell packing by 96 h. Co-culture with MΦ2 disrupted spheroid formation entirely: intact SKOV-3/MΦ2 spheroids did not form, and instead multiple small, irregular aggregates were observed (Video 4). In Model b (Fig. 1B), where immune cells were added 24 h after spheroid formation, ThP-1 monocytes rapidly accumulated around the pre-formed SKOV-3 spheroid, giving rise to a thick peripheral corona by 96 h (Video 5). MΦ also localized around the spheroid initially but gradually intermingled with SKOV-3 cells over time (Video 6). In contrast, MΦ1 remained largely restricted to the periphery, maintaining a distinct outer layer even at 96 h (Video 7). MΦ2 adhered to the spheroid surface after 24 h and progressively integrated into the structure; however, a subset of MΦ2 cells formed small independent clusters surrounding the main spheroid at later time points (Video 8). Spheroid diameter quantification (Fig. 1C and D for *Model a* and *b*) shows a highly significant ($p < 0.001$) overall reduction of spheroid size compared to SKOV-3 in presence of macrophages. Video analysis performed to visualize 3D distribution of immune cells throughout the spheroids reveals a more marked cell-to-cell interaction following *Model a* (Fig. 1E) compared to *Model b* (Fig. 1F), with MF populations reaching the center of the spheroid and ThP-1 cells are also being able to permeate the spheroid.

Simplified organotypic cultures of cancer cells and exos from immune cells

Due to the phenotypic changes in spheroid formation and structure observed following the addition of different macrophage types, we tested the potential role of EXOs isolated from immune cells (ThP-1 monocytes, MF, MF1 or MF2) in influencing spheroids formation. Fluorescently labelled (PKH67) ThP-1-, MF, MF1 or MF2-derived EXOs were mixed with SKOV-3 cells (labelled with PKH26) to form spheroids. Spheroid growth was monitored at 24 and 48 h. Spheroids formed in presence of EXOs following *Model a* and *Model b* revealed that EXOs did not alter spheroid phenotype in the same way parental cells did (Fig. 2A).

EXOs had the capacity to penetrate through the spheroid after 24 h (Supplementary Fig. 3A, Supplementary Fig. 4A) and distribute evenly across it after 48 h (Supplementary Fig. 3B, Supplementary Fig. 4B). In all cases EXOs were found to accumulate at the core of the spheroid (the highest values were recorded at z-stacks Z4 and Z5, respectively), and appeared to be present in a higher concentration after 48 compared to 24 h. Histograms in Fig. 2C and D show the quantification of the mean fluorescent intensity signal associated to EXOs at 24 and 48 h, respectively, following both Models. At 24 h, at higher concentration of EXOs was observed upon addition of MF1- and MF2-derived EXOs following *Model b*, compared to *Model a*. The curves generated from the 3D projections of the confocal z-Stacks confirmed EXOs are found at the core of spheroid at 24 h, with *Model b* determining an increased accumulation towards the center of the spheroid compared to *Model a* (Fig. 2Ca). Fluorescence signals reach comparable levels between models at 48 h (Fig. 2Cb). A more marked accumulation was found when EXOs from macrophagic populations were mixed, since ThP-1-EXOs only displayed a deem fluorescent signal at 48 h following *Model a*.

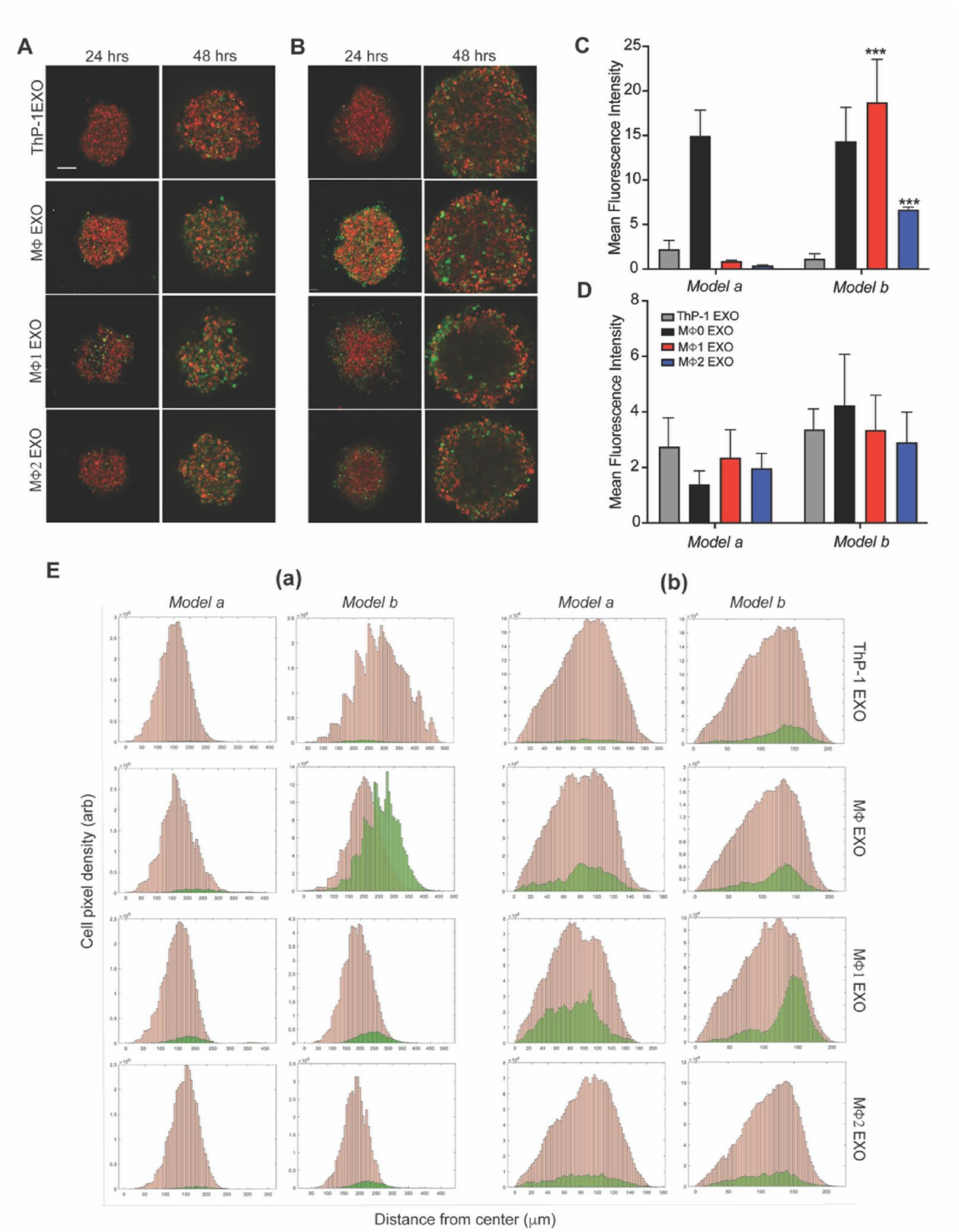

Fig. 2 Organotypic culture of SKOV-3 and immune cell-derived exosomes. SKOV-3 cells and EXOs were fluorescently labelled with PKH26 (red) and PKH67 (green), respectively. Exosomal suspensions were added at time 0 (**A**) and after 24 h from spheroid formation (**B**), Pictures were taken using an Olympus FV3000 after 24 and 48 h from exosomal addition. Confocal pictures taken after 24 h from cell seeding: 20X Magnification, scale bar: 150 µm. Confocal pictures taken after 48 h from cell seeding: 40X magnification, scale bar: 75 µm. Mean Fluorescent Intensity signal obtained from PKH67 (green) quantified using ImageJ software at 24 h (**C**) and 48 h (**D**) from EXO addition following Model a and Model b. Results from three independent biological replicates are shown. Statistical significance determined comparing Model b versus Model a (***$p < 0.001$). (**E**) Histograms showing the distribution of EXOs from immune cells across the spheroids following *Model a* and *Model b* after 24 (**a**) and 48 (**b**) hrs, determined by evaluating the fluorescence intensity relative to the 3D Euclidean distance from the center of the spheroid (generated by projecting the z-planes onto a half sphere) at the latest time point. Green and red lines depict SKOV-3 and immune cells, respectively

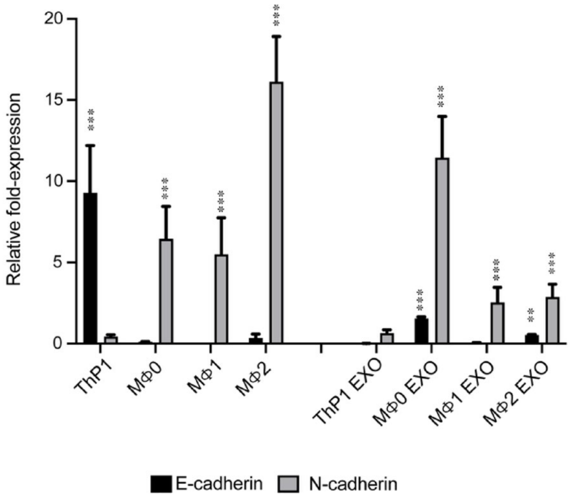

Fig. 3 Effect of direct and indirect interaction of immune cells on spheroid EMT-associated genes. Expression of E-CAD and N-CAD expression were measured on spheroid formed by exposing SKOV-3 cells to immune cells (ThP-1, MF, MF1, and MF2) or their exosomal counterparts. Target gene values were normalized to the house-keeping gene GAPDH. Markers were further normalized to provide fold expression for direct comparison with 3D SKOV-3 only spheroids. Results from three independent biological replicates are shown (***$p < 0.001$)

Expression of genes associated to epithelial-to-mesenchymal transition

To evaluate whether the macroscopic changes observed in the spheroids following exposure to immune cells or immune cells-derived EXOs correspond to changes in expression of the EMT markers, E-Cadherin (E-CAD) and N-cadherin (N-CAD) gene expression analysis was undertaken (Fig. 3). Analysis of E-CAD expression at 48 h in the combined tumor and immune cells model (*Model a)* showed an overall significant decrease in the expression of E-CAD *c*ompared to the SKOV-3 only spheroids, with expression values for SKOV-3/MF of 0.11 ± 0.02, $p < 0.001$, and close to zero for SKOV-3/MF1 and SKOV-3/MF2 ($p < 0.001$). In the case of N-CAD expression, a significant increase in expression was seen upon exposing SKOV-3 cells to macrophages, with MF and MF1 showing a similar trend (6.45 ± 2.24- and 5.5 ± 2.78-fold increase, respectively) ($p < 0.001$). The presence of MF2 stimulated a 3-fold increase in N-CAD expression compared to MF and MF1 populations, with values assessed around 16.12 ± 2.78 ($p < 0.001$). The expression of cadherins induced following exposure of spheroids to EXOs showed little to no E-CAD expression in SKOV-3/ThP-1 (0.009 ± 0.01-fold increase), MF1 (0.05 ± 0.02-fold increase) and MF2 (0.54 ± 0.03-fold increase) EXO-exposed spheroids, while a slight increase was noticed when SKOV-3 were exposed to MF-EXOs (1.5 ± 0.09-fold increase). On the other hand, the presence of EXOs from macrophages was found to cause a significant increase in N-CAD expression, with values determined as 11.46 ± 2.52, 2.53 ± 0.93, and 2.87 ± 0.78 for MF-, MF1-, and MF2-EXOs, respectively ($p < 0.001$).

DISCUSSION

Treating OC poses significant challenges, particularly due to cancerous cell clusters detaching from the primary tumor into the ascites that can establish multiple metastatic niches and to the tumor immune microenvironment (TIME) established at these metastatic sites, with altered physical properties that foster an immunosuppressive milieu [35]. Spheroids formed through the co-culturing of OC cells with immune cells represent valuable models that recapitulate the complex interactions that occur within the ascites and TIME and enables the investigation of various aspects of OC progression, including tumor growth, invasion, immune evasion, and response to therapy [36–38]. Through the optimization of a preclinical model utilizing the mouse ovarian surface epithelial cell line (ID-8), we recently investigated the immune landscape established within the peritoneal cavity during advanced OC, focusing on both tumor mass and ascites accumulation. Our data unveiled the presence of T cells and antigen-presenting cells (including macrophages) dispersed within tumor nodules along the peritoneal membrane [22]. Consistent with this body of data, the present study aimed to investigate the role of monocytes/macrophages in OC spheroid formation. To achieve this, simplified organotypic spheroids containing both OC cells (SKOV-3 cell line) and various subsets of monocytes/macrophages were generated in vitro[37] and their interaction monitored over time. We used two distinct approaches: Model a, where immune cells are co-seeded with tumor cells from time 0, and Model b, where immune cells are added 24 h after spheroid formation. Our data demonstrate that these models yield distinct spheroid characteristics. For example, co-cultures with THP-1 monocytes resulted in spheroids characterized by a dense outer layer of monocytes, while spheroids generated with differentiated macrophages (MF, MF1, MF2) exhibited unique interaction patterns that influenced spheroid size and compactness. The combination of ThP-1 monocytes and SKOV-3 cells resulted in spheroids characterized by a dense outer layer of monocytes enveloping the inner core of tumor cells. This observation suggests that monocytic cells infiltration into TME may be hindered, as the result of elevated levels of immunosuppressive molecules or altered expression of cell adhesion molecules [39], which are often associated to immune evasion [40, 41] and tumor progression [42]. Although this behavior may be attributed to the close aggregation of the OC cell type chosen for this study [43], it is noteworthy that this phenomenon was observed both when monocytes were added to SKOV-3 cells at the outset (time 0) and after 24 h. This suggests a time-independent impact on spheroid formation and a distinct exclusion of monocytic cells from the clustering process compared to the behavior observed when macrophages were introduced. These findings align with the differential adhesion hypothesis, which postulates that the organization and compaction of multicellular structures are influenced by differences in adhesion molecule expression among interacting cell types [44]. The exclusion of monocytic cells from the spheroid core and their tendency to form an external layer may reflect intrinsic disparities in cell-cell adhesion properties between immune cells and SKOV-3 cells, as well as dynamic changes in adhesion molecule expression that dictate cellular positioning within the spheroid over time [45]. Furthermore, the evaluation of adhesion molecule expression revealed a marked increase ($p < 0.001$) in E-CAD in this experimental group, concomitantly with a basal N-CAD expression compared to SKOV-3 only spheroids or spheroids exposed to macrophage subpopulations. This trend also diverges from findings reported in the literature concerning monocyte infiltration in 3D multicellular spheroids formed using cell lines derived from various cancer types, such as breast and pancreatic cell lines [46]. Authors reported monocytes rapidly infiltrate spheroids and differentiate into mature macrophages with diverse phenotypes in a cancer cell line-dependent manner.

Although the widely accepted MF1/MF2 dichotomy has been expanded since a transcriptomic analysis uncovered a spectrum of different TAM functional states, MF1 and MF2 can still be regarded as the two ends of this continuum of phenotypes, in which different subpopulations can hold both, MF1 and MF2 features [47]. Compared to their pro-inflammatory MF1 counterparts, MF2 are predominant in the OC TME and have been associated with immunosuppressive roles such as the inhibition of T cell proliferation [48] or the secretion of immunosuppressive cytokines such as CCL17, CCL22 and IL-10 [49, 50]. TAM presence in ovarian carcinoma has been correlated with poor survival rates [51] and represents a potentially relevant target for the development of effective treatments. As an example, regulating chemoattractant factors known to recruit macrophages into the ovarian TME is a promising approach for reducing tumor infiltration of TAMs [35]. When we examined the impact of different macrophage subpopulations (including MF, MF1 and MF2) distinct patterns emerged in spheroid formation, reflecting the roles these immune cell types play within the OC environment. Consistent with existing literature showing macrophages being able to infiltrate 3D cancer spheroids [52], we observed differences in cell-cell interaction comparing to ThP-1 cells, upon mixing MF and MF1 with SKOV-3 cells, which were contingent on the model employed for 3D structure formation. With *Model a*, both MF or MF1 directly engaged with SKOV-3 cells, resulting in spheroids that became smaller and more compact over time. The observed reduction in size induced by MF1 agrees with the pro-inflammatory role these cells play and in line with a body of evidence suggesting their potential tumoricidal activities [53]. The addition of MF determined a delay in spheroid organization that was found to be functional to the formation of a more compact entity, even in comparison to MF1-induced counterparts. Conversely, following *Model b* a distinct behavior was observed, whereby immune cells (both MF and MF1 macrophages) surrounded the spheroid by 24 h. Notably, while MF were able to infiltrate the structure to some extent, MF1 appeared less adept at penetrating the spheroid, maintaining a distinct, well-defined layer around it even after 96 h. On the other hand, in line with previously reported evidence suggesting their involvement in initiating the metastatic process [38, 54–56], the presence of MF2 resulted in the formation of multiple spheroids of varying size, deviating from the typical rounded spheroid morphology with both Models. The concomitant addition of MF2 macrophages and tumor cells determined the formation of a large cluster, surrounded by smaller clusters over time. These smaller clusters became larger overtime, due to a continuous interplay occurring between entities, as shown in Videos 4 and 8. The addition of MF2 after 24 h from spheroid formation led to the development of an external corona around tumor cells and few small aggregates of immune cells in the surroundings. Cell exchange between aggregates determined the formation of mixed spheres, a process initiated by MF2. The interplay between MF2 and cancer cells for spheroid formation has been described by Long et al. showing the presence of TAMs inducing a more aggressive phenotype of cancer cells [57].

Previous studies showed that TAMs infiltrate advanced tumors where EMT is induced in cancer cells [58]. To elucidate the contribution of macrophage presence in SKOV-3 phenotype and measure differences between experimental groups, the expression of markers involved in EMT was evaluated, by focusing on E-CAD and N-CAD expression. We observed a three-fold increase in N-CAD expression, particularly in the presence of MΦ2, although E-CAD levels were low across all experimental groups. It is important to note that EMT is a complex process involving additional transcription factors such as Snail, Slug, ZEB1/2, and Twist 8 and that ovarian cancer cells may exhibit partial or reversible EMT states. *N-cad* has been associated with tumor invasiveness and poor survival in OC [59], its role remains controversial [60] and should be interpreted with caution in this context. Concomitantly, the absent to low levels of E-CAD aligns with the notion that metastasis-prone epithelial OC cells gradually undergo a decrease in the expression levels of this gene to prepare for detachment from the primary tumor site and abdomen invasion [61], leading to adverse clinicopathological features. Driven by studies showing the potential of macrophage-derived EXOs to influence tumor progression and immune responses within the TME [62], we hypothesized that the observed effect could be mediated by paracrine signals exchanged between cell types. To test this hypothesis, SKOV-3-based organoid structures were developed replacing immune cells with their EXOs and monitored over 48-hr periods. Our observation indicated that EXOs distribute uniformly among cancer cells when incubated with them following *Model a*. Additionally, they successfully penetrate spheroids when introduced after spheroid formation. The tendency of EXOs to overcome biologic barriers by virtue of their nanoscopic size compared to their parental has been widely described [63–65], with macrophage-derived EXOs being able to regulate tumorigenesis through crosstalk with surrounding cells [66]. While no phenotypical changes were observed at a macroscopic level across groups, the analysis of EMT markers within the different spheroid types revealed a pattern of expression that is similar to the one observed upon cell co-culturing. A marked increase in the expression of N-CAD was observed as consequent to the exposure of SKOV-3 spheroid to EXOs from macrophagic cells. Surprisingly, the MF group showed the highest N-CAD expression levels. While the expression of N-CAD in macrophages is in line with data obtained with their cellular counterparts, a discrepancy between our findings and existing literature exists, since greater N-CAD expression levels have been reported for MF2 compared to MF [67]. The observed difference could be due to variations in the types of cancer cells and models used in those earlier studies.

In our current study, the exposure to macrophages and their derived exosomes leads to a significant increase in N-cadherin expression in SKOV-3 spheroids, suggesting an EMT-like shift in the tumor cells. Notably, this observation aligns with our recent findings where we demonstrated that adipocyte-tumor interactions -investigated through both cell line models and patient-derived samples - also promote a cadherin switch characterized by elevated N-cad levels [68]. These parallel results indicate that distinct stromal components within the tumor microenvironment, such as adipocytes and macrophages, may converge on similar molecular pathways to enhance mesenchymal traits and tumor invasiveness. Together, these studies underscore the critical role of microenvironmental cues in modulating tumor cell plasticity and highlight the therapeutic potential of targeting the signaling pathways underlying this cadherin switch. Our results with EXOs suggest they are mediators of the observed molecular alterations found in SKOV-3 cells exposed to macrophagic populations. Several miRNAs carried by macrophage-derived EXOs have been implicated in OC progression, by specifically targeting genes involved in cell proliferation migration, and invasion [69]. The observed differences in EXO size, concentration and behavior across macrophage genotypes can be attributed to several factors related to macrophage biology [64, 70]. Different macrophage genotypes exhibit distinct activation states, metabolic profiles, and secretory pathways, all of which influence exosome biogenesis, cargo loading, and release dynamics [71]. Variations in cytokine signaling, intracellular trafficking mechanisms, and membrane composition could also contribute to these differences. Besides miRNAs, circular RNAs (circTMCO3) have been recently identified as exosomal moieties elicited by MF2 to promote malignancy in OC [72]. The molecular interplay between cell types and the impact of cancer cells to macrophage phenotype should be also addressed since hypoxic EOC cells have been reported to induce a TAM-like phenotype, and that EXOs derived from macrophages were able to deliver miR-223 to EOC and to confer them drug-resistance (i.e., cisplatin) through the activation of the PTEN-PI3K/AKT pathway both in vitro and in vivo [73]. Further studies into the role of exosomal moieties will unveil additional insights into the crosstalk between cancer cells and macrophages within spheroids to better understand the phenotypical changes observed in the spheroids which are not related to 'classical' EMT, including their capability to enhance stem-like properties in cancer cells. It is worth nothing that our bulk transcriptomic analysis in a co-culture system may partly reflect changes in cellular composition rather than pure tumor cell reprogramming.

Future work employing cell-sorting or single-cell RNA sequencing, coupled with a broader panel of EMT markers, will be necessary to fully delineate the processes observed in our models. Furthermore, while circularity provided a convenient 2D metric of spheroid compactness, it has clear limitations in capturing the full 3D architecture. To address this, we plan to incorporate volume-based analyses in future studies for a more comprehensive characterization of spheroid morphology. Finally, we recognize that the use of SKOV-3 cells and ThP-1–derived MΦ in this proof-of-concept study does not fully capture the complexity of OC and its immune microenvironment. As a next step, validation using additional OC cell lines (e.g., IGROV1) and integration of primary patient-derived immune populations will be critical to strengthen the translational value of our models and to bridge controlled in vitro systems with clinically relevant tumor–immune interactions.

Recent advances in spatial transcriptomics further highlight the critical role of tissue organization in understanding ovarian cancer biology. For instance, Stur et al. used intact tissue spatial transcriptomics to reveal that tumor and stromal cluster architecture, rather than composition alone, correlates with chemotherapy response in HGSOC [74]. More recently, Denisenko et al. identified discrete tumor subclones with distinct ligand–receptor signaling neighborhoods, suggesting subclone-specific interactions with immune, stromal, and endothelial populations [75]. In parallel, a radiogenomics study by Ju et al. integrated CT imaging with spatial transcriptomics and demonstrated the potential for non-invasive stratification of recurrent vs. non-recurrent disease [76]. These findings reinforce that physical context and spatial proximity are key determinants of tumor–immune dynamics and therapeutic response. Our spheroid models, by recapitulating controlled spatial configurations of tumor and immune cells, offer an experimentally tractable platform to probe these organization-dependent mechanisms and complement insights from patient tissue spatial profiling.

Conclusion

Our research highlights the significant role of MΦ and their EXOs in shaping the cellular dynamics and functionality of OC spheroid models. The dual-model approach adopted in this study demonstrates that early co-aggregation versus later immune cell infiltration exerts distinct effects on spheroid morphology, adhesion molecule expression, and EMT-like shifts in tumor cells. By focusing on E- and N-cadherin, we provided an initial indication of epithelial–mesenchymal dynamics; however, we acknowledge that a broader analysis of EMT-related genes will be important to fully delineate these processes. Aligning our findings with our prior in vivo analyses of ascites immune landscapes, we propose that *Model a* more closely reflects the compact, mixed aggregates observed in ascites-bearing OC mice, whereas *Model b* mimics the later infiltration or exclusion of immune cells into established tumor clusters [22]. This distinction underscores that the two models are not redundant but instead capture complementary stages of tumor–immune interactions. Together, our results support the role of MΦ as active contributors to the tumor microenvironment and point to their interactions with tumor cells as promising therapeutic targets. While this study serves as a proof-of-concept, it establishes a framework for future validation using additional ovarian cancer cell lines and patient-derived samples, thereby strengthening its translational relevance.

Abbreviations

CCL2	C-C Motif chemokine ligand 2
CCL17	C-C Motif chemokine ligand 17
CCL22	C-C Motif chemokine ligand 22
CD	Cluster of differentiation
cDNA	Complementary DNA
circTMCO3	Circular RNA TMCO3
CXCL10	C-X-C Motif Chemokine ligand 10
E-CAD	E-cadherin
EMT	Epithelial-to-mesenchymal transition
EOC	Epithelial ovarian cancer
EXOs	Exosomes
FBS	Fetal bovine serum
HEPES	4-(2-Hydroxyethyl)-1-piperazineethanesulfonic acid
HGSOC	High-grade serous ovarian cancer
IFN-γ	Interferon Gamma
IL	Interleukin
LPS	Lipopolysaccharide
miRNA	MicroRNA
mRNA	Messenger RNA
MΦ	Macrophages
MΦ1	Pro-inflammatory macrophages
MΦ2	Anti-inflammatory macrophages
N-CAD	N-cadherin
OC	Ovarian cancer
PBS	Phosphate-buffered saline
PI3K/AKT	Phosphoinositide 3-kinase/protein kinase B
PTEN	Phosphatase and tensin homolog
P/S	Penicillin/streptomycin
SKOV-3	Serous ovarian cancer cell line
TAM	Tumor-associated macrophages
TME	Tumor microenvironment
ThP-1	Human monocyte cell line
TNF-α	Tumor necrosis factor alpha

Supplementary Information

The online version contains supplementary material available at https://doi.org/10.1186/s12967-025-07162-2.

Supplementary Material 1

Supplementary Material 2

Supplementary Material 3

Supplementary Material 4

Supplementary Material 5

Supplementary Material 6

Supplementary Material 7

Supplementary Material 8

Acknowledgements

SP was sponsored by the Swansea University Medical School (UK)/Houston Methodist Research Institute (US) joint PhD Initiative.

Author contributions

SP: conducted experimental work, collected and analyzed the data, contributed to the interpretation of data; contributed to drafting the manuscript, and approved the final version of the manuscript. YSJ: conducted experimental work, collected the data, and approved the final version of the manuscript. PR: collected and analyzed the data and approved the final version of the manuscript. JX: assisted with data collection and analysis; contributed to writing sections of the manuscript; and approved the final version of the manuscript. DG: contributed to the interpretation of data and approved the final version of the manuscript. RSC: Provided critical revisions to the manuscript and approved the final version of the manuscript. BC: conceived and designed the work, supervised the research project, wrote the manuscript.

Funding

Support for the study was provided by the Golfers Against Cancer Foundation to BC.

Data availability

The datasets used and/or analyzed during the current study are available from the corresponding author on reasonable request.

Declarations

Ethics approval and consent to participate
Not applicable.

Consent for publication
Not applicable.

Competing interests
The authors declare that they have no competing interests. The authors declare no conflict of interest regarding this paper's publication.

Received: 18 July 2025 / Accepted: 11 September 2025

References

1. Labidi-Galy SI, et al. High grade serous ovarian carcinomas originate in the fallopian tube. Nat Commun. 2017;8(1):1093.
2. Sohn MH, et al. Classification of high-grade serous ovarian carcinoma by epithelial-to-mesenchymal transition signature and homologous recombination repair genes. Genes. 2021. https://doi.org/10.3390/genes12071103.
3. Blake Gilks C, Singh N. Synchronous carcinomas of endometrium and ovary: a pragmatic approach. Gynecol Oncol Rep. 2019;27:72–3.
4. Tadic V, Zhang W, Brozovic A. The high-grade serous ovarian cancer metastasis and chemoresistance in 3d models. Biochim Biophys Acta Rev Cancer. 2024;1879(1):189052.
5. Jimenez-Sanchez, A., et al., *Heterogeneous Tumor-Immune Microenvironments among Differentially Growing Metastases in an Ovarian Cancer Patient.* Cell, 2017. **170**(5): p. 927–938 e20.
6. Christofi T, et al. Current perspectives in cancer immunotherapy. Cancers (Basel). 2019. https://doi.org/10.3390/cancers11101472.
7. Liu Z, et al. Immunosuppression in tumor immune microenvironment and its optimization from CAR-T cell therapy. Theranostics. 2022;12(14):6273–90.
8. Mei S, et al. Tumor microenvironment in ovarian cancer peritoneal metastasis. Cancer Cell Int. 2023;23(1):11.
9. Kodack DP, et al. Primary patient-derived cancer cells and their potential for personalized cancer patient care. Cell Rep. 2017;21(11):3298–309.
10. Yee C, et al. Three-dimensional modelling of ovarian cancer: from cell lines to organoids for discovery and personalized medicine. Front Bioeng Biotechnol. 2022;10:836984.
11. Akerlund E, et al. The drug efficacy testing in 3D cultures platform identifies effective drugs for ovarian cancer patients. NPJ Precis Oncol. 2023;7(1):111.
12. Sokolova E, et al. Penetration efficiency of antitumor agents in ovarian cancer spheroids: the case of recombinant targeted toxin DARPin-LoPE and the chemotherapy drug, doxorubicin. Pharmaceutics. 2019. https://doi.org/10.3390/pharmaceutics11050219.
13. Ribatti D, Tamma R, Annese T. Epithelial-mesenchymal transition in cancer: a historical overview. Transl Oncol. 2020;13(6):100773.
14. Ford CE, et al. The untapped potential of ascites in ovarian cancer research and treatment. Br J Cancer. 2020;123(1):9–16.
15. Almeida-Nunes DL, et al. Immune tumor microenvironment in ovarian cancer ascites. Int J Mol Sci. 2022. https://doi.org/10.3390/ijms231810692.
16. Mikula-Pietrasik J, et al. Malignant ascites determine the transmesothelial invasion of ovarian cancer cells. Int J Biochem Cell Biol. 2017;92:6–13.
17. Ding Y, et al. Molecular characteristics and tumorigenicity of ascites-derived tumor cells: mitochondrial oxidative phosphorylation as a novel therapy target in ovarian cancer. Mol Oncol. 2021;15(12):3578–95.
18. Ahmed N, Thompson EW, Quinn MA. Epithelial-mesenchymal interconversions in normal ovarian surface epithelium and ovarian carcinomas: an exception to the norm. J Cell Physiol. 2007;213(3):581–8.
19. Shield K, et al. Multicellular spheroids in ovarian cancer metastases: biology and pathology. Gynecol Oncol. 2009;113(1):143–8.
20. Engelberg JA, Ropella GE, Hunt CA. Essential operating principles for tumor spheroid growth. BMC Syst Biol. 2008;2:110.
21. Cui X, Hartanto Y, Zhang H. Advances in multicellular spheroids formation. J R Soc Interface. 2017. https://doi.org/10.1098/rsif.2016.0877.
22. Pisano S, et al. Assessment of the immune landscapes of advanced ovarian cancer in an optimized in vivo model. Clin Transl Med. 2021;11(10):e551.
23. Yin M, et al. Tumor-associated macrophages drive spheroid formation during early transcoelomic metastasis of ovarian cancer. J Clin Invest. 2016;126(11):4157–73.
24. Raghavan S, et al. Ovarian cancer stem cells and macrophages reciprocally interact through the WNT pathway to promote pro-tumoral and malignant phenotypes in 3D engineered microenvironments. J Immunother Cancer. 2019;7(1):190.
25. Han C, et al. Exosome-mediated communication between tumor cells and tumor-associated macrophages: implications for tumor microenvironment. Oncoimmunology. 2021;10(1):1887552.
26. Chen, X., et al., *Corrigendum to "Exosomes derived from hypoxic epithelial ovarian cancer cells deliver microRNAs to macrophages and elicit a tumor-promoted phenotype" [Cancer Lett. 435 (28 October 2018) 80–91].* Cancer Lett, 2023. **568**: p. 216292.
27. Cummings M, Freer C, Orsi NM. Targeting the tumour microenvironment in platinum-resistant ovarian cancer. Semin Cancer Biol. 2021;77:3–28.
28. Hansen JM, Coleman RL, Sood AK. Targeting the tumour microenvironment in ovarian cancer. Eur J Cancer. 2016;56:131–43.
29. Rojas A, et al. HMGB1 enhances the protumoral activities of M2 macrophages by a RAGE-dependent mechanism. Tumour Biol. 2016;37(3):3321–9.
30. Carlsson J, Yuhas JM. Liquid-overlay culture of cellular spheroids. Recent Results Cancer Res. 1984;95:1–23.
31. Yang M, et al. Macrophage phenotypic subtypes diametrically regulate epithelial-mesenchymal plasticity in breast cancer cells. BMC Cancer. 2016;16:419.
32. Taylor DP, et al. Hepatic nonparenchymal cells drive metastatic breast cancer outgrowth and partial epithelial to mesenchymal transition. Breast Cancer Res Treat. 2014;144(3):551–60.
33. Pisano S, et al. Immune (Cell) derived exosome mimetics (IDEM) as a treatment for ovarian cancer. Front Cell Dev Biol. 2020;8:553576.
34. Vaiasicca S, et al. Transcriptomic analysis reveals the anti-cancer effect of gestational mesenchymal stem cell secretome. Stem Cells Transl Med. 2024. https://doi.org/10.1093/stcltm/szae024.
35. Yang Y, et al. Tumor microenvironment in ovarian cancer: function and therapeutic strategy. Front Cell Dev Biol. 2020;8:758.
36. Thongsin N, Wattanapanitch M. A three-dimensional immune-oncology model for studying in vitro primary human NK cell cytotoxic activity. PLoS ONE. 2022;17(3):e0264366.
37. Yang M, et al. Diverse functions of macrophages in different tumor microenvironments. Cancer Res. 2018;78(19):5492–503.
38. Schweer D, et al. Tumor-associated macrophages and ovarian cancer: implications for therapy. Cancers (Basel). 2022. https://doi.org/10.3390/cancers14092220.
39. Lambrechts D, et al. Phenotype molding of stromal cells in the lung tumor microenvironment. Nat Med. 2018;24(8):1277–89.
40. Joyce JA, Fearon DT. T cell exclusion, immune privilege, and the tumor microenvironment. Science. 2015;348(6230):74–80.
41. Chen DS, Mellman I. Elements of cancer immunity and the cancer-immune set point. Nature. 2017;541(7637):321–30.
42. Salmon H, et al. Matrix architecture defines the preferential localization and migration of T cells into the stroma of human lung tumors. J Clin Invest. 2012;122(3):899–910.
43. Tofani LB, et al. Establishment and characterization of an in vitro 3d ovarian cancer model for drug screening assays. Biotechnol Prog. 2020;36(6):e3034.
44. Foty RA, Steinberg MS. The differential adhesion hypothesis: a direct evaluation. Dev Biol. 2005;278(1):255–63.
45. Niessen CM, Leckband D, Yap AS. Tissue organization by cadherin adhesion molecules: dynamic molecular and cellular mechanisms of morphogenetic regulation. Physiol Rev. 2011;91(2):691–731.
46. Madsen NH, et al. Monocyte infiltration and differentiation in 3D multicellular spheroid cancer models. Pathogens. 2021. https://doi.org/10.3390/pathogens10080969.
47. Xue J, et al. Transcriptome-based network analysis reveals a spectrum model of human macrophage activation. Immunity. 2014;40(2):274–88.
48. Galdiero MR, et al. Tumor associated macrophages and neutrophils in tumor progression. J Cell Physiol. 2013;228(7):1404–12.
49. Nowak M, Klink M. The role of tumor-associated macrophages in the progression and chemoresistance of ovarian cancer. Cells. 2020. https://doi.org/10.3390/cells9051299.
50. Gordon SR, et al. PD-1 expression by tumour-associated macrophages inhibits phagocytosis and tumour immunity. Nature. 2017;545(7655):495–9.

51. Truxova I, et al. Targeting tumor-associated macrophages for successful immunotherapy of ovarian carcinoma. J Immunother Cancer. 2023. https://doi.org/10.1136/jitc-2022-005968.
52. Singh K, Gautam PK. Macrophage infiltration in 3D cancer spheroids to recapitulate the TME and unveil interactions within cancer cells and macrophages to modulate chemotherapeutic drug efficacy. BMC Cancer. 2023;23(1):1201.
53. Gu Z, et al. Ferroptosis-strengthened metabolic and inflammatory regulation of tumor-associated macrophages provokes potent tumoricidal activities. Nano Lett. 2021;21(15):6471–9.
54. Zhang M, et al. A high M1/M2 ratio of tumor-associated macrophages is associated with extended survival in ovarian cancer patients. J Ovarian Res. 2014;7:19.
55. Reinartz S, et al. Mixed-polarization phenotype of ascites-associated macrophages in human ovarian carcinoma: correlation of CD163 expression, cytokine levels and early relapse. Int J Cancer. 2014;134(1):32–42.
56. Worzfeld T, et al. The unique molecular and cellular microenvironment of ovarian cancer. Front Oncol. 2017;7:24.
57. Long L, et al. Tumor-associated macrophages induced spheroid formation by CCL18-ZEB1-M-CSF feedback loop to promote transcoelomic metastasis of ovarian cancer. J Immunother Cancer. 2021. https://doi.org/10.1136/jitc-2021-003973.
58. Liu Q, et al. Emodin reduces breast cancer lung metastasis by suppressing macrophage-induced breast cancer cell epithelial-mesenchymal transition and cancer stem cell formation. Theranostics. 2020;10(18):8365–81.
59. Assidi M. High N-Cadherin protein expression in ovarian cancer predicts poor survival and triggers cell invasion. Front Oncol. 2022;12:870820.
60. Zisis T, et al. Disentangling cadherin-mediated cell-cell interactions in collective cancer cell migration. Biophys J. 2022;121(1):44–60.
61. Onder TT, et al. Loss of E-cadherin promotes metastasis via multiple downstream transcriptional pathways. Cancer Res. 2008;68(10):3645–54.
62. Zhao Y, et al. Docetaxel-loaded M1 macrophage-derived exosomes for a safe and efficient chemoimmunotherapy of breast cancer. J Nanobiotechnology. 2022;20(1):359.
63. Conlan RS, et al. Exosomes as reconfigurable therapeutic systems. Trends Mol Med. 2017;23(7):636–50.
64. Corradetti B, et al. Editorial: Exosomes as therapeutic systems. Front Cell Dev Biol. 2021;9:714743.
65. Wang D, et al. Crosstalk between N6-methyladenosine (m6A) modification and noncoding RNA in tumor microenvironment. Int J Biol Sci. 2023;19(7):2198–219.
66. Zhou M, et al. Exosome derived from tumor-associated macrophages: biogenesis, functions, and therapeutic implications in human cancers. Biomark Res. 2023;11(1):100.
67. Guo Y, et al. M2 Tumor Associate Macrophage- (TAM-) Derived lncRNA HISLA Promotes EMT Potential in Bladder Cancer. Journal of Oncology. 2022;2022:8268719.
68. Williams ME, et al. Adipocyte derived exosomes promote cell invasion and challenge paclitaxel efficacy in ovarian cancer. Cell Commun Signal. 2024;22(1):443.
69. Wang P, et al. Exosomes from M1-polarized macrophages enhance paclitaxel antitumor activity by activating macrophages-mediated inflammation. Theranostics. 2019;9(6):1714–27.
70. Gharavi AT, et al. The role of macrophage subtypes and exosomes in immunomodulation. Cell Mol Biol Lett. 2022;27(1):83.
71. Liu M, et al. The role of exosomal molecular cargo in exosome biogenesis and disease diagnosis. Front Immunol. 2024;15:1417758.
72. Ran XM, et al. M2 macrophage-derived exosomal circTMCO3 acts through miR-515-5p and ITGA8 to enhance malignancy in ovarian cancer. Commun Biol. 2024;7(1):583.
73. Zhu X, et al. Macrophages derived exosomes deliver miR-223 to epithelial ovarian cancer cells to elicit a chemoresistant phenotype. J Exp Clin Cancer Res. 2019;38(1):81.
74. Stur E, et al. Spatially resolved transcriptomics of high-grade serous ovarian carcinoma. iScience. 2022;25(3):103923.
75. Denisenko E, et al. Spatial transcriptomics reveals discrete tumour microenvironments and autocrine loops within ovarian cancer subclones. Nat Commun. 2024;15(1):2860.
76. Ju HY, et al. Integrated analysis of spatial transcriptomics and CT phenotypes for unveiling the novel molecular characteristics of recurrent and non-recurrent high-grade serous ovarian cancer. Biomark Res. 2024;12(1):80.

Publisher's note